Chapter 3

Spin-up conversion and magnetization dynamics in La_2NiMnO_6

3.1 Introduction

This chapter focuses on the multiple magnetic transitions, spin-up conversion, and dynamics study of LNMO crystallites. The LNMO samples were obtained by post-thermal reaction of a refined powder after a solid reaction of La_2O_3, NiO, and MnO_2. A sintered LNMO of a pellet was crushed into tiny pieces, and ball milled (with hard ZrO_2 balls) in ethanol for 10 h (S_1), 15 h (S_2), and 25 h (S_3), so as it fractures, deforms, and grows in refined facets of small crystallites having core-shell structure [92, 93]. The ball milling increases cations mixings and decreases the size (providing higher surface area during further calcination). The spin-up $Ni^{2+} \rightarrow Ni^{3+}$: d^7 and $Mn^{4+} \rightarrow Mn^{3+}$: d^4 conversion and charge transfer in small core-shell crystallites were investigated. Four types of spin orders occur in an exchange-coupled magnet over allied T_{c1}*, T_{c1}, T_{c2}, or T_{SG} transitions. That has duly tuned on thermal anneals of a master sample, described with X-ray diffraction (XRD) and lattice images. The presence of charge valences is demonstrated by X-ray photo-electron spectroscopy. A frustrated magnetic state is explored by field-dependent magnetic irreversible in ZFC/FC (zero field-cooled and field-cooled) magnetization (M), heating-cooling cycles. Due to randomness and frustration, magnetic interactions become weaker and can be easily affected by the external magnetic field. Cole-Cole plots at different frequencies are used to determine the collective relaxation of spins. Electron spin resonance spectroscopy (ESR) also studied collective spin dynamics. Model relations describe the spin dynamics in terms of enthalpy and entropy in coupled spin phonons over elevated temperatures.

Bulk LNMO is a ferromagnetic (FM) insulator usually contains La^{3+}, Ni^{2+} and Mn^{4+} cations (phase-1) ordering via O^{2-} in octagons maintaining charge neutrality in a double perovskite [53, 61]. It is a unique example of multiple functionalities that can be tuned in terms of the spins, charge carriers, or polarons via magnetic and or electric field [26, 94–100]. An induced $Ni^{2+} \rightarrow Mn^{4+}$ electron transfer causes unpaired spins $3d^8 \rightarrow 3d^7$-(Ni^{3+}) and $3d^3 \rightarrow 3d^4$-(Mn^{3+}) via O^{2-} ligands of a more vital FM phase-2— leading to tailored magnetic, electronic and photonic properties on revived charge carriers [11, 65, 88, 101–105]. A spin-density ρ_s = 0.7 s a^{-1} (spins per atom) arises over the initial Ni^{2+}/Mn^{4+} species (phase-1), ρ_s = 0.5 s a^{-1}, *i.e.* 2.12 μ_B/f.u. larger spin-moment. The LNMO is well studied in bulk [26, 53, 104], nanostructure [65, 94, 98, 102], or thin-films [95, 97, 105]. Recent studies mainly focus on exploring its magnetic [11, 26, 53, 61, 65, 88, 94–105], magnetodielectric [26, 61, 96],magnetoresistance [61, 99], ferroelastic/ferroelectric [101, 104], photocatalysis [11, 98], optical [11, 95] properties for multiple technologies as nonvolatile memories, energy-storage, actuator/transducer, medical tools, photonics, etc [11, 65, 88, 101–105]. The LNMO has a viable module that conducts charge-spin function united in multiferroics by manipulating the electron-spin-phonon coupling in multifunctional devices [26, 53, 61, 94–98].

Generally, Ni^{2+} and Mn^{4+} ions in LNMO occupies two different crystallographic sites BO_6 and $B^{'}O_6$ type polygons, respectively, bonding via O^{2-} in a joint FM network, with a Curie temperature $T_{c1} \cong 280$ K [61, 94–96]. Accordingly, fewer Ni^{2+} and Mn^{4+} cations can flip over antisites B and $B^{'}$ in a typical pseudo-cubic ABO_3 phase (A = La and $B \leftrightarrow B^{'}$), on revived are Mn^{4+}-O^{2-}-Mn^{4+}, Ni^{2+}-O^{2-}-Ni^{2+}, Mn^{3+}-O^{2-}-Mn^{3+} or Ni^{3+}-O^{2-}-Ni^{3+} ligands [26, 95, 96]. The 3d-spins in the antisites Mn^{4+}-O^{2-}-Mn^{4+} and Ni^{2+}-O^{2-}-Ni^{2+} setup oppositely in an antiferromagnet (AFM) [11, 26, 88, 95–103], indulging a frustrated lattice, and turn in a lower net saturation magnetization (M_s). As a result, a long FM order breaks down into smaller spin clusters of Ni-O-Mn multiple valences. As a result, two separate T_C transitions, *e.g.* $T_{c1} \cong 270$ K, $T_{c2} \cong 138$ K in LNMO thin films [95], appear in the account of two types Ni^{2+}-O^{2-}-Mn^{4+} and Ni^{3+}-O^{2-}-Mn^{3+} spintronics, respectively [94, 95]. Further, an SG-like behavior, freezing at $T_g \cong 50$ K in a bulk sample [26, 103], refined clusters of cold spins rather readily trap (randomly) in large entropy in coupled phonons.

3.2 Results and discussion

3.2.1 Growth of small core-shell

Figure (3.1) describes a typical XRD pattern of sample S_3 of all peaks are indexed well with their d_{hkl} (interplanar spacing) values, for monoclinic crystal structure ($P2_1/n$ space group) [103]. A small difference (blue line) between observed (black open circle) and calculated (red lines) values confirms an ordered LNMO phase-1 of small crystallites. A little NiO [106] $\leqslant 2$ mol%, has grown of a (220) XRD peak, $d_{220} = 0.1485$ nm; a reinforced FM-AFM composite of tunable spintronic, catalysis, and other useful properties [107–109]. Table (3.1) tabulate the lattice parameters and crystallite size of different samples. A 'compressive surface effect' has been observed with different size in samples. As given in Table (3.1) consistently, a duly smaller $V_c \equiv 0.2311$ nm^3, or $\rho = 7.005$ g cm^{-3} is reported of LNMO grown in smaller D = 66 nm via a sol-gel route. In O^{2-} deficits $B(B^{'})O_n$ units, n < 6, confine in shorter $B(B^{'})$ -O^{2-} bonds with β twisting closer to 90°. An equilibrium value $V_c \cong 0.2333$ nm^3, or $\rho = 6.939$ g cm^{-3}, return on filling O^{2-} vacancies in the regular oxide polygons, $n \rightarrow 6$; a bulk LNMO, *i.e.* the equilibrium FM phase-1 of Mn^{4+} and Ni^{2+} species.

The most intense XRD peak Fig. (3.1) contains three overlappings (200), (112), and (020) peaks, as marked on a zoomed scale in the inset, which varies in positions and relative intensities from $S_1 \rightarrow S_3$ samples. Thus, LNMO has grown primarily in a $\langle 112 \rangle$ texture, which shares a maximum (112) peak intensity as per a large $\langle 112 \rangle$ cross-sectional area in the individual crystallites. (200) peak is slowly grown over (020) peak instead of involving effectively larger number density of (200) lattices.

Table 3.1 Structural parameter of small core-shell LNMO crystallites.

Sample	Lattice parameters				c/a	V_c	ρ_c	D
	a (nm)	b (nm)	c (nm)	β(°)		(nm^3)	(g/cm^3)	(nm)
S_1	0.5521	0.5479	0.776	90.01	1.4055	0.2347	6.898	65
S_2	0.5524	0.5482	0.7763	90.01	1.4053	0.2351	6.886	75
S_3	0.5525	0.5484	0.7767	90.02	1.4058	0.2353	6.88	80
Nano[1]	0.5515	0.543	0.775	90	1.4053	0.2311	7.005	66
Bulk[1]	0.5512	0.5462	0.7751	90.29	1.4062	0.2333	6.939	-

[1] indicates values obtained from references [94, 103]

The studies of SEM images insight surface topology of LNMO has multiple shapes of its permeable facet of small crystallites. It dictates the reaction path and its kinetics. For instance, SEM images in Figures (3.2) display a clear effect of milling on refining size,

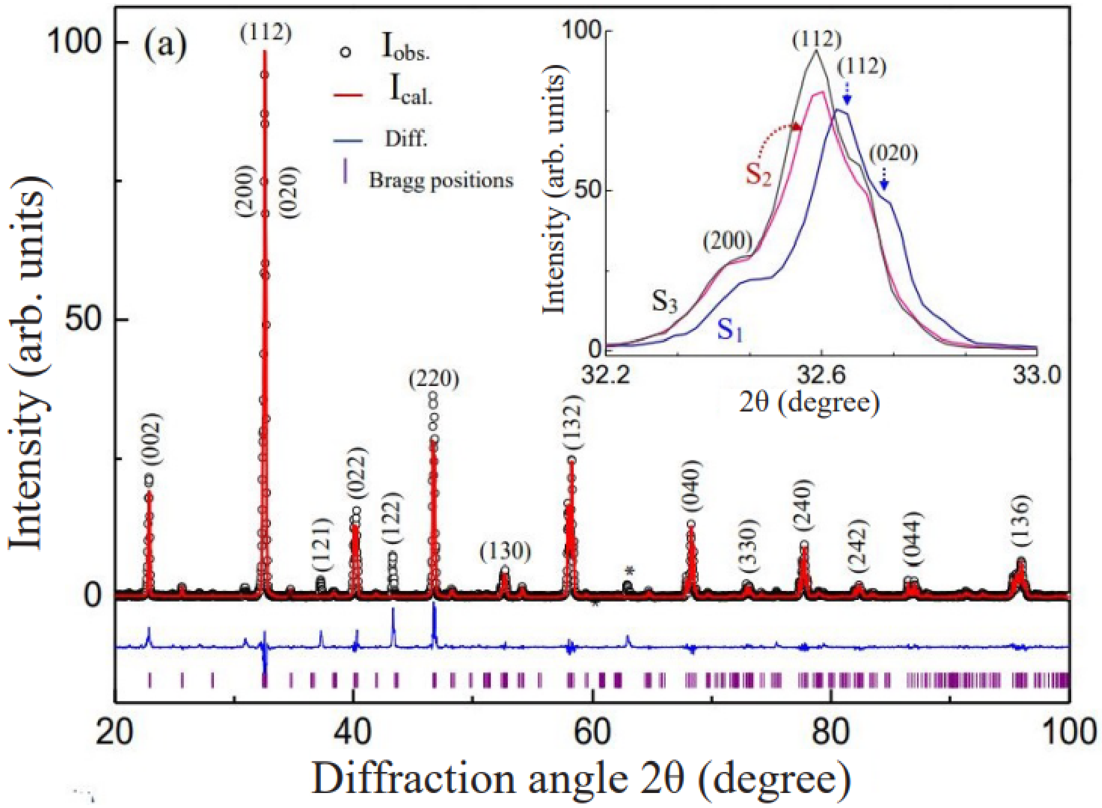

Fig. 3.1 Observed (points) and Rietveld refined (line) XRD peaks of LNMO (sample S_3), their difference (blue line), a standard stick pattern (bottom), Inset shows the variation in intense peak.

shape, and topology in these samples. Thin platelets (W = 0.5–1.5 μm widths and δ = 50–150 nm depths) shown in sample S_1 are grown as oblates (W = 0.5–1.5 μm and δ = 0.2–2 μm) of oval facets in S_2 and S_3 samples. The histograms in Figure (3.3) plot the size distribution of plates in the SEM images. A Gaussian fit to the data (marked by solid curves) presents 1.02. 1.15 and 1.28 μm mean sizes in three samples, respectively.

Figure (3.4(a, b)) shows typical HRTEM images of core–shells of a distinct shell bonding over thin plates LNMO (W = 100-200 nm) of a bright peripheral (ϑ =2-3 nm thickness) from sample S_3. The shell interlinks the cores in a joint hierarchical structure. Part of a plate A (Fig. (3.4(b))) zoomed-in Fig. (3.4)(c) insights a clear core-shell interface bonding in an oval shape, as also shown in the SEM images in Fig. (3.2). Uniquely, atomic arrays have locally bent upon the core in a truncated shape of $BB^{'}O_n$, n $\leq$ 6, network. A model (in the inset) projects how (112) arrays in Fig. (3.4(d)) have displaced off near edges in small spikes and setup at different angles in a cluster. It anticipates self-order in a short array and recovers positions in the surface to an interior zone B in a graded structure. So, long (112) arrays run through undisrupted in regime B (Fig. (3.4(e))), with a regular

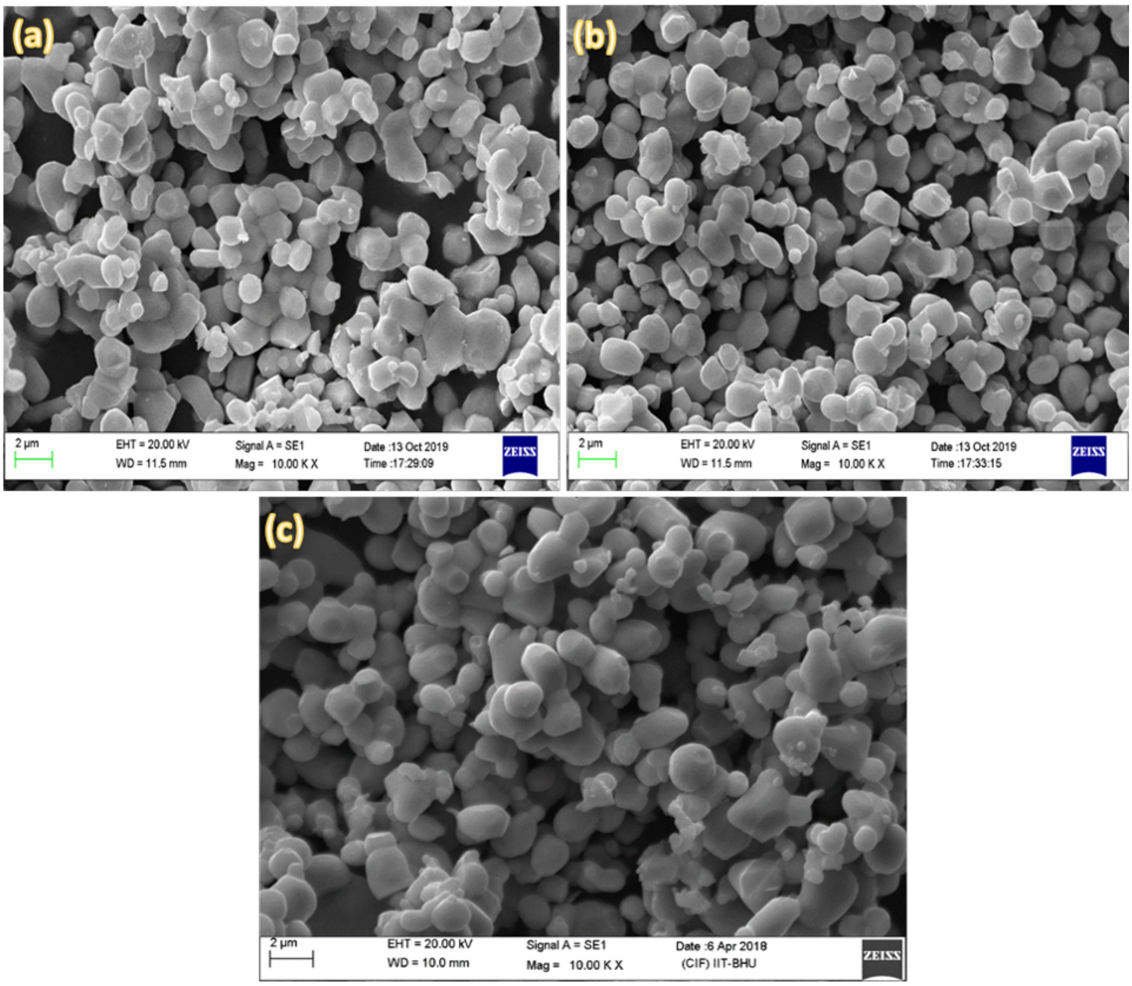

Fig. 3.2 SEM images of different shapes LNMO in (a) S_1, (b) S_2 and (c) S_3 samples.

separation d_{112} = 0.2745 nm, which opts an equilibrium value 0.2755 nm (shown in the XRD in Fig. (3.1)).

As mutual interaction grows, smaller core-shells LNMO (W = 10-20 nm) more effectively blend in a dense cluster, which is shown in the HRTEM images Figure (3.5(a)) or sample S_1. Mapping a shell separately is not easy for such samples. It is feasible in separately grown core–shells as shown in Fig. (3.5(b)). Otherwise, while imaging in an electron beam is used, small core–shells travel to come closer and adjoin more intimately in a rigid cluster. A shell, $\vartheta \sim 0.5$ nm, shown in a laminate A (20 nm × 10 nm cross-section—a core) in the inset, shares a roughly 15 vol % at $\delta \cong 5$ nm. In Fig. (3.5(c)), (002) lattice arrays, d_{002} = 0.3875 nm, in region. A display over small strips (or fringes) of a disordered phase —a surface strained layer. (112) arrays in region B, zoomed

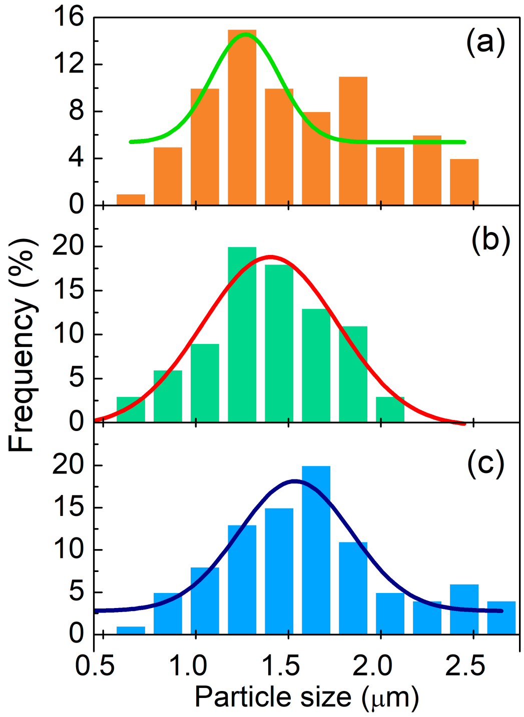

Fig. 3.3 Particle size distributions in (a) S$_1$, (b) S$_2$ and (c) S$_3$ samples determined from SEM images in Fig. 3.2, showing an average size of 1.02, 1.15 and 1.28 μm, respectively.

in the inset (d) (Fig. (3.5(c))), are inclined at 45° over (002) arrays, zoomed in the inset (e) (Fig. (3.5(c))), in a net-like structure. A duly distorted lattice is reflected in (002) arrays, which have locally bent in region C in an oblate at an angle 8° (marked thereon) over the unperturbed zone A. Likely, it infers an antisite Mn^{4+} (Ni^{2+}) inclusion, displacing a fewer Ni^{2+} as NiO on the (002) arrays (as seen in the XRD in Fig. (3.5)), which forms a twin (a blister) in a reinforced composite phase.

3.2.2 Valence state determination

Figure (3.6(a)) shows the XPS survey scan for crystallites S$_1$ acquired at room temperature. The presence of O, Mn, Ni, and La in LNMO is clearly detected. The XPS spectra were fitted with the Shirley background for all types of crystallites S$_1$, S$_2$, and S$_3$. O-*1s* core-level XPS spectrum consists of a doublet peak with intensity at energies 529.4 eV and 531.3 eV as shown in Fig. (3.6(b)). The peak at 529.4 eV corresponds to lattice oxygen (O$_I$), and the peak at 531.3 eV corresponds to surface oxygen (O$_{II}$) [65, 110–113]. The surface oxygen is increasing compared to lattice oxygen as one change from sample S$_1$

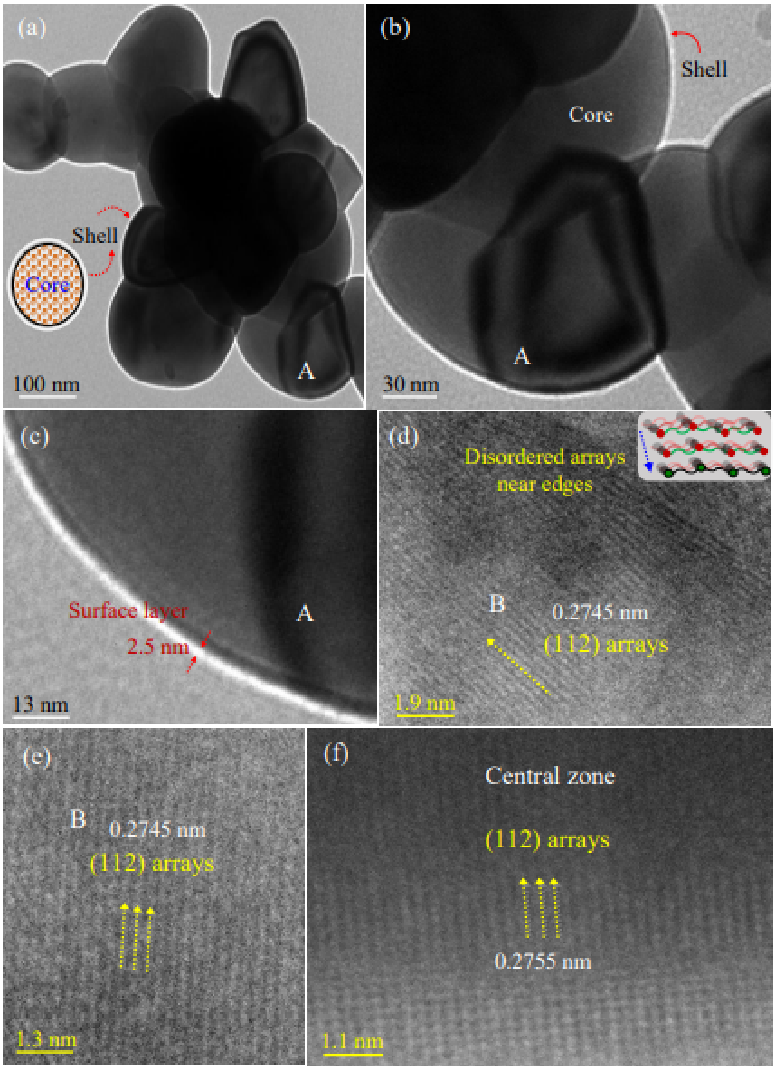

Fig. 3.4 (a, b, c) HRTEM images of a core-shell LNMO zoomed at different scales (S_3), showing lattice arrays varied (d) near edges (gradually displaced off positions of atoms projected in a model in the inset), (e) below edges.

to S_3 indicates an enhanced oxygen vacancy (see Table (3.2)). The oxygen vacancies distort the unit cell and deviate the bond angle 180° super-exchange interaction between Ni^{2+}-O^{2-}-Mn^{4+}. The higher oxygen vacancies are reported earlier by Gaikwad *et al.* [65]; these will play a part in changing the bond angle between Ni-O-Mn or distorting unit cells. Fig. (3.6(c)) shows the Mn-$2p$ core-level spectrum across the binding energy of 630-660 eV that represents the Mn-$2p_{3/2}$ and Mn-$2p_{1/2}$ peaks. The binding energy positions around 641 eV (Mn-$2p_{3/2}$) and 653 eV (Mn-$2p_{1/2}$) attributed to Mn^{3+} valence state, while the peak at 643 eV (Mn-$2p_{3/2}$) and 656 eV (Mn-$2p_{1/2}$) are ascribed to Mn^{4+} [65, 110–114]. XPS spectrum for Mn exhibits a shoulder feature referred to as a charge transfer peak

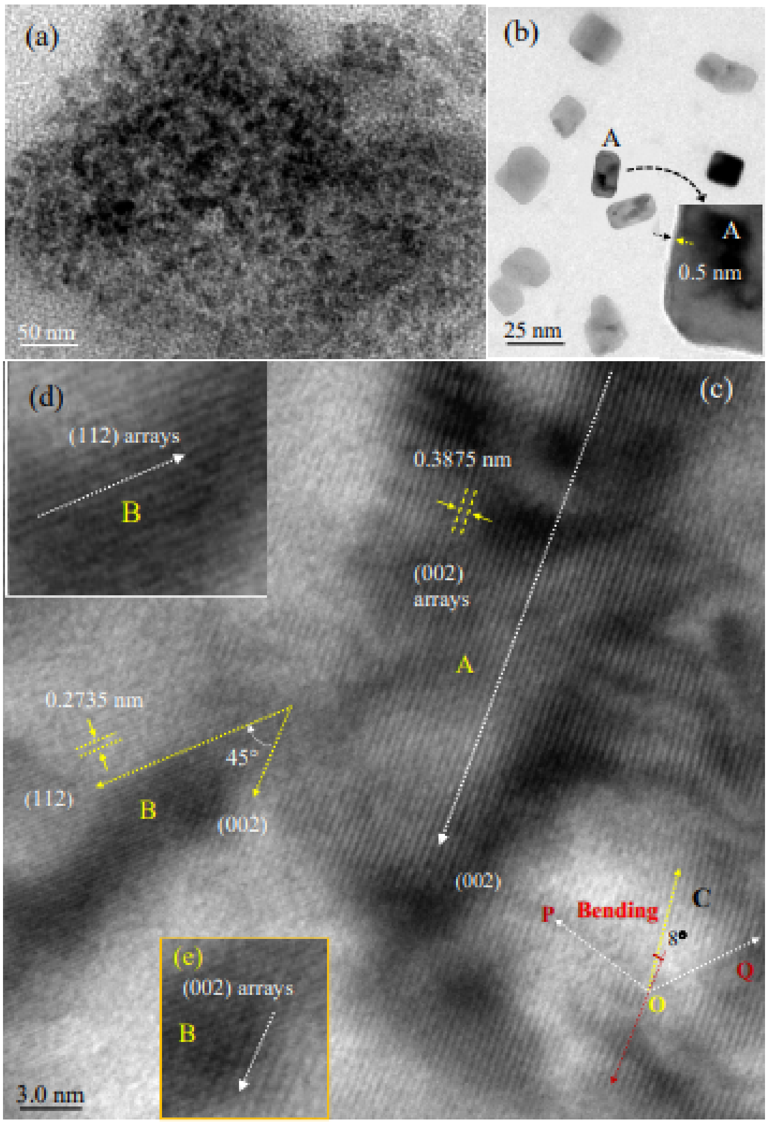

Fig. 3.5 (a, b) HRTEM images of LNMO (S$_1$) and (c) (002) lattice arrays enclosed in a (112) surface (regions A and B) at an angle 45°, as zoomed in the insets (d, e). The (002) arrays are curled near edges C in an oval shape.

recorded across ∼637.0 eV [113]. The relative intensities of the shoulder are compared in inset Fig. (3.6(a)).

Fig. (3.6(d)) shows the core-level XPS spectrum of Ni-*2p* that overlapped with the La-*3d* spectrum. The overall Ni-*2p* and La-*3d* XPS spectra have deconvoluted into multiple peaks. Two bands were detected across 850 eV that correspond to La-$3d_{3/2}$ (∼850 eV) and Ni-$2p_{3/2}$ (∼851 eV) [65, 110–114]. The peak around ∼851 eV is assigned to the 2+ valence state of Ni-$2p_{3/2}$, while the peak around ∼855 eV to Ni^{3+} (Ni-$2p_{3/2}$). The XPS

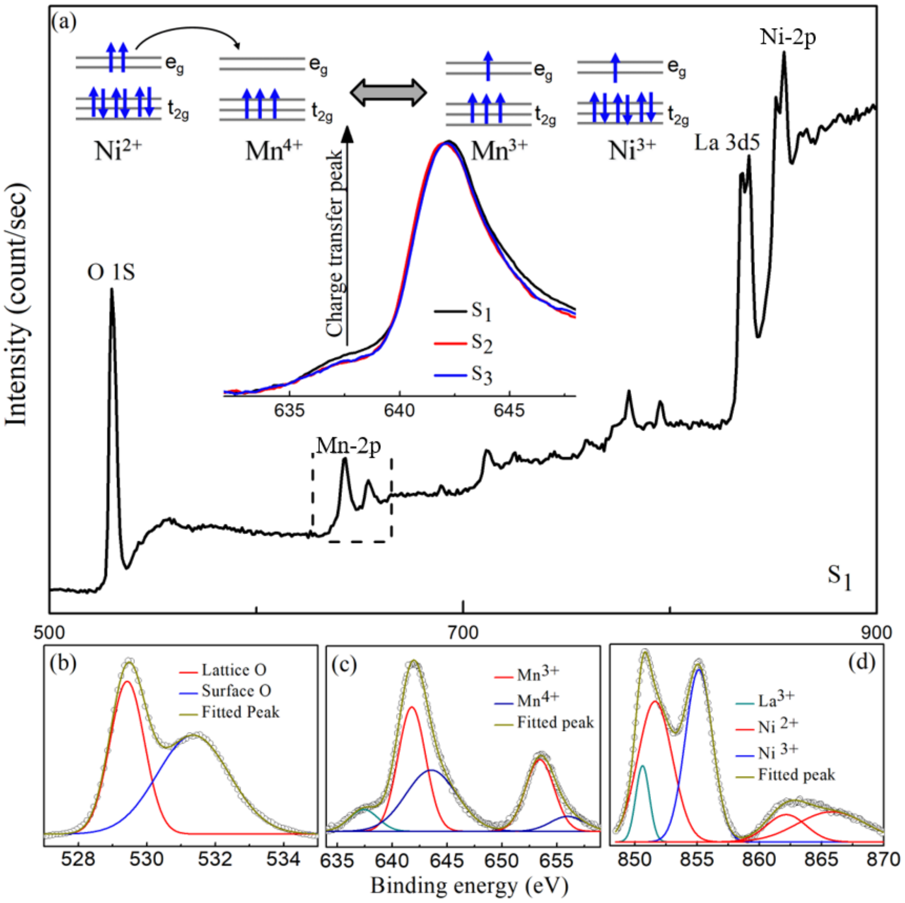

Fig. 3.6 (a) XPS survey for sample S_1, inset show normalized intensity for Mn-*2p*, and charge transfer (b) O-*1s*, (c) Mn-*2p*, (d) Ni-*2p* overlapped with La-*3d* spectra for specimen crystallites S_1.

spectra analysis of crystallites S_1, S_2, and S_3 confirm the presence of different cations valence states of Ni and Mn, and their relative fractions are determined by the relative peaks area ratio (see Table (3.2)). The oxygen vacancies can be estimated by considering the charge neutrality of samples. Ni and Mn possessed oxidation states of 2.49 and 3.40 for S_1, 2.45 and 3.38 for S_2, and 2.45 and 3.37 for S_3. The estimated fractions of Ni and Mn for all crystallites and their chemical formula based on charge neutrality are shown in Table (3.2). A relatively higher fraction of Mn^{3+} and Ni^{3+} suggests a stronger ordering of Mn^{3+}-O^{2-}-Ni^{3+} than Mn^{4+}-O^{2-}-Ni^{2+} or higher strength of T_{c2} than T_{c1}. The presence of different charge cations leads to $Mn^{4+} + Ni^{2+} \rightarrow Ni^{3+} + Mn^{3+}$ charge transfer or vice versa. The inset of Fig. (3.6(a)) shows a weaker spectral weight from S_1 to S_3, suggesting that larger crystallite sizes have lower charge transfer. Particles with a larger crystallite size have a smaller surface area or a weaker Ni and Mn interaction than those with a smaller crystallite size. Controlling cation distribution and interactions in this complex oxide system is difficult, which plays a crucial role in magnetic, electric, and optical properties. The presence of different charge valencies increases the distortion of the unit cell due to multiple connecting octahedra centers having different sizes of cations. This charge conversion layer can be understood as a core-shell structure of LNMO crystallites [12], where the evolution of defects, distortions, and stresses on the surface helps in the transfer of electrons (spin) so that the shell has a different phase compared to bulk (core). Therefore, core-shell has different magnetic structures or spin configurations. If the core is compared as a domain where the surface has Ni^{2+} ion (antisites), charge transfer occurs via electron and hole transfer across Mn^{4+} ion (antisites).

Table 3.2 Chemical valence state for LNMO crystallites.

Sample	Ni^{2+}	Ni^{3+}	Mn^{3+}	Mn^{4+}	Chemical Composition
S_1	0.51	0.49	0.60	0.40	$La_2(Ni^{2+}_{0.51}Ni^{3+}_{0.49})(Mn^{3+}_{0.60}Mn^{4+}_{0.40})O_{5.945}$
S_2	0.55	0.45	0.62	0.38	$La_2(Ni^{2+}_{0.55}Ni^{3+}_{0.45})(Mn^{3+}_{0.62}Mn^{4+}_{0.38})O_{5.915}$
S_3	0.55	0.45	0.63	0.37	$La_2(Ni^{2+}_{0.55}Ni^{3+}_{0.45})(Mn^{3+}_{0.63}Mn^{4+}_{0.37})O_{5.910}$

3.2.3 Magnetization study in small core-shell crystallites

A core-shell LNMO - a soft magnet reveals an exchange-coupled magnetization in a symmetric M–H loop at low temperatures, $T < T_{c2} \leqslant 150$ K Figure (3.7) displays how the M–H plot, as zoomed-in the inset (a), differs in S_1, S_2 and S_3 samples, as measured over H = ± 20 kOe fields at 5 K. No net magnetization saturates (M_s) until this much fields, instead of the surface spins, have canted at multiple facets at different angles and rotates slowly along an induced M-H on the core, which in turn slowly turns along the applied field H in a conjoint magnet. In this case, the M_s can be stipulated by extrapolating M-H over high-field susceptibility (χ_m) in a law of approach to saturation [115].

$$M = M_s\left[1 - \frac{4}{15}\frac{K_1^2}{M_s^2H^2}\right] + \chi_m H \tag{3.1}$$

As H tends to infinity, a nonlinear χ_m(H) extends over H-induced rotation and displacements of surface spins following an average anisotropy field, $H_a = 2K_1/M_s$ in the FM and/or AFM phases. As given in Table (3.3), an M_s = 30.5 emu g^{-1} (coercivity H_c = 205

Oe) obtained at 5 K in sample S_1 is duly enhanced, 53.8 emu g^{-1} (H_c = 130 Oe), in sample S_2, which is a bit diluted to 52.7 emu g^{-1} (H_c = 125 Oe) on surface-spin largely canting in multiple facets in sample S_3. An optimized M_s = 53.8 emu g^{-1} (4.70 μ_B/f.u.) in this work is thus very close to M_s = 56.8 emu g^{-1} (H_c = 300 Oe) known for bulk LNMO —a pure FM phase-1 [61]. Adversely, M_s is known to fall down to 17.6 emu g^{-1} on reducing D $\leq$ 80 nm; a counterpart effect of unsaturated surface-spins [94, 98]. An antisites $Ni^{2+} \leftrightarrow Mn^{4+}$ disorder further lowers M_s, *e.g.* 13.8 emu g^{-1} known in bulk [103], or 17.6 emu g^{-1} in nanoplates [94]. Uniquely, a larger M_s = 72.2 emu g^{-1} (H_c = 130 Oe) prevails in LNMO nanorods (20 nm diameter and 120 nm length) [65]. In principle, a large M_s 53.8 emu g^{-1} is a result of the high spin ρ_s phase-2 of small core-shell crystallites. As a fact, an average M_s hardly falls in small crystallites. In general, it is the surface topology that duly controls high H_c and other nontrivial properties in collective dynamics of spins in a core-shell of reversed single magnetic domains at critical size (D_c) as follows.

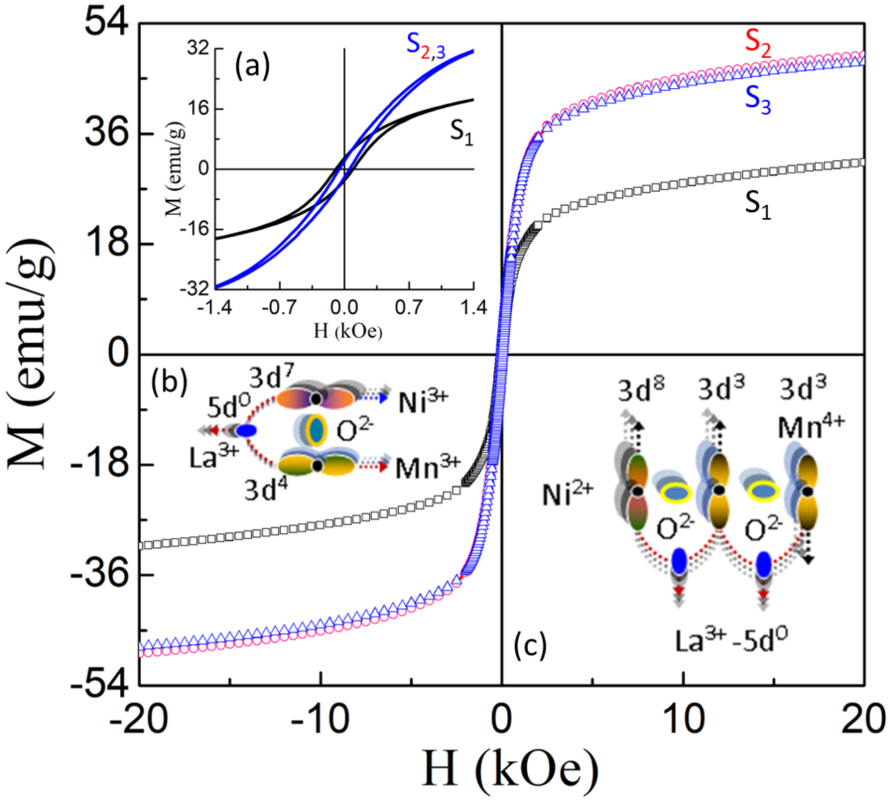

Fig. 3.7 Magnetic hysteresis loops of LNMO samples S_1, S_2, and S_3 at 5 K, exhibiting (a) a small H_c magnified in the (inset), with model spin-lattices in (b) a $Ni^{2+} \rightarrow Mn^{4+}$ electron-transfer, (c) an antisite Mn^{4+} inclusion.

Now, let us view magnetism in a long-range ordered LNMO phase-1 of spins. The $3d^8$–Ni^{2+} and $3d^3$–Mn^{4+} spins order parallel via O^{2-} ions (net spins S = 0) of an FM phase, which reveals a net magnetic moment,

$$\begin{aligned}\mu_{s1} &= g_1 s_1 N_1 (N_1+1)^{1/2}\mu_B + g_2 s_2 N_2 (N_2+1)^{1/2}\mu_B \\ &\cong 2.694\mu_B + 3.464\mu_B \\ &\cong 6.16\mu_B\end{aligned}$$

Assuming the Lande g-factor $g_1 = 2.2$, $g_2 = 2.0$, $s_1 = s_2 = 1/2$ free-electron spin, and number of free spins $N_1 = 2$ for Ni^{2+}, while $N_2 = 3$ for Mn^{4+} ions. It is a maximum pliable value (theoretical) in this phase-1 what is it tuned in the nanorods [65]. It arises to $\mu_{s2} \cong$ 8.28 μ_B/f.u., with $N_1 = 3$ and $N_2 = 4$ on an electron transfer Ni^{2+} -O^{2-} -Mn^{4+} to Ni^{3+} -O^{2-} -Mn^{3+} in FM phase-2. Here, we must consider an orbital moment μ_l of $La^{3+}(5d^0)$-a xenon like filled electron-shell (diamagnetic: DM), which controls the net value,

$$\begin{aligned}\mu_{sl} &= \left[\mu_s^2 + \mu_l^2 \pm 2\mu_s\mu_l cos\varphi\right]^{1/2} \\ &\cong \mu_s - \mu_l, \quad as \;\; \varphi \rightarrow 180^\circ \\ &\geq 4.96\mu_B\end{aligned}$$

of ordered phase-1, with μ_l = (-)1.2 μ_B, i.e. 0.6 μ_B per La^{3+} ion, on a theoretical μ_s = 6.16 μ_B value. In a support, in fact μ_{sl} rises by 0.4 μ_B per Mn^{4+} on La^{3+} deficiencies [116]. In general, an angle φ varies, $90^\circ \leq \varphi \leq 180^\circ$ between μ_s and μ_l vectors to cope a net μ_{sl} value. A small Ni^{3+} –O^{2-} –Mn^{3+} inclusion, $\mu_{s2} \cong$ 8.28 μ_B/f.u., thus would lead to raise a value μ_{sl}, as observed in the nanorods [65] in a hybrid FM phase-2. A similar μ_l = (-) 0.27 μ_B/Bi favors K_1 in a uniaxial $Mn_{0.5}Bi_{0.5}$ magnet [117–119]. A micromagnetic model in Fig. (3.7(b)) describes how a La^{3+} –$5d^0$ shell keeps Ni^{3+} and Mn^{3+} spins aligned via O^{2-} in a stable FM phase over its μ_l value in a tripod. Adversely, an antisite Mn^{4+} (or Ni^{2+}) spin setups oppositely to its adjacent sites in a lattice, so as the net μ_{sl} drops in an FM – AFM composite [118, 119], but it favours H_c [95, 97] and ferroics [101] in thin films. In Fig. (3.7(c)), a model describes the spins setup in support of a DM field of La^{3+} and O^{2-} species. Qualitatively, it describes well M_s widely vary in LNMO, usually 17–72 emu g^{-1} (Table (3.3)), as per its microstructure. A counterpart DM anticipates lower M_s as it grows over FM in smaller crystallites. A spin-lattice $La_2(Ni_{1-x}Mn_x)_A(Mn_{1-x}Ni_x)_BO_6$ of an antisite Ni ↔ Mn(x) disorder has its own limit, $x \leq 0.5$, in this structure. The part $(Ni_{1-x}Mn_x)$ retains an FM order, while the other Ni_xMn_x converts in an AFM, order of an exchange coupled magnet,

$$\underset{DM}{\downarrow La_2} \; \underset{FM}{\{Ni_{1-x}Mn_{1-x}\} \uparrow\uparrow} \; \underset{AFM}{\{Ni_xMn_x\} \uparrow\downarrow} \; \underset{DM}{O_6 \downarrow}$$

Here, the arrows mark the respective sites' upward and downward magnetic moments. At x = 0.5, a minimum μ_{sl} = 1.88 μ_B/f.u. (21.5 emu g^{-1}) incurs in the low-spin phase-1, which arises to 2.94 μ_B/f.u. (33.7 emu g^{-1}) in the higher spin phase-2, presuming a model μ_l = (-) 0.6 μ_B/La^{3+}, as described above. These model μ_{sl} values can fall down further in presence of other spin defects and/or SPM (superparamagnet) species in small spin clusters, *e.g.* as small as 1.2 μ_B/f.u. observed in a disordered LNMO, a bulk sintered phase [103].

As measured over 5-200 K, the ZFC-FC curves (Fig. (3.8)) bifurcate at T < T_{c2}, and exhibits a sharp T_{c2} peak in their derivatives (in the right), in lieu of the high-spin phase-2 ($\mu_{s2} \cong$ 8.28 μ_B/f.u.) stabilized in LNMO small crystallites. As given in Table (3.3), T_{c2} $\cong$ 105 K has grown from sample S_1 to at 146 K in sample S_2, or 148 K in sample S_3. Plausibly, it rises led by enthalpy ΔH_m (area in the peak), $T_{c2} \cong \Delta H_m(\Delta S_m)^{-1}$, in a case the spin-entropy ΔS_m no longer grows in bigger crystallites [120, 121]. It anticipates $\Delta V_c \cong 0.3\%$ enhanced V_c (Table (3.1)), *i.e.* proportional to ΔH_m in the first law of thermodynamics. Also, ZFC-FC magnetization irreversibility is dropped as surface effect of spins drops below a critical value in later samples. Further, the magnetization flops in an inflection in spins freezing randomly at T < $T_{SG} \cong$ 8 K, 22 K, or 24 K in ZFC, *i.e.* duly shifted to at 23 K, 23 K, or 24 K in FC in the respective samples. In a magnetic memory [121, 122], the surface-spins lagging reversibility in sample S_1. A similar type of spin cluster, as described in a model in Fig. (3.7(c)), also arises on an antisite FM → AFM disorder in bulk LNMO [26, 103] *i.e.* freezing at T $\leq T_{SG} \cong$ 42 K [121, 122].

In a simple model, small core-shells in a spin-cluster modulate its spin dynamics over T_{SG} in two basic variants vibrational (ΔS_v) and configurational (ΔS_c) entropies,

$$T_g \cong \frac{\Delta H_{vc}}{\Delta S_v - \Delta S_c} \tag{3.2}$$

where ΔH_{vc} is the counterpart enthalpy value. A soft phonon of an harmonic oscillator of frequency 'ν' of a lattice shares an entropy [123, 124],

$$\Delta S_v(T) \cong k_B ln \left\{ \frac{k_B T}{h\nu} + 1 \right\} \tag{3.3}$$

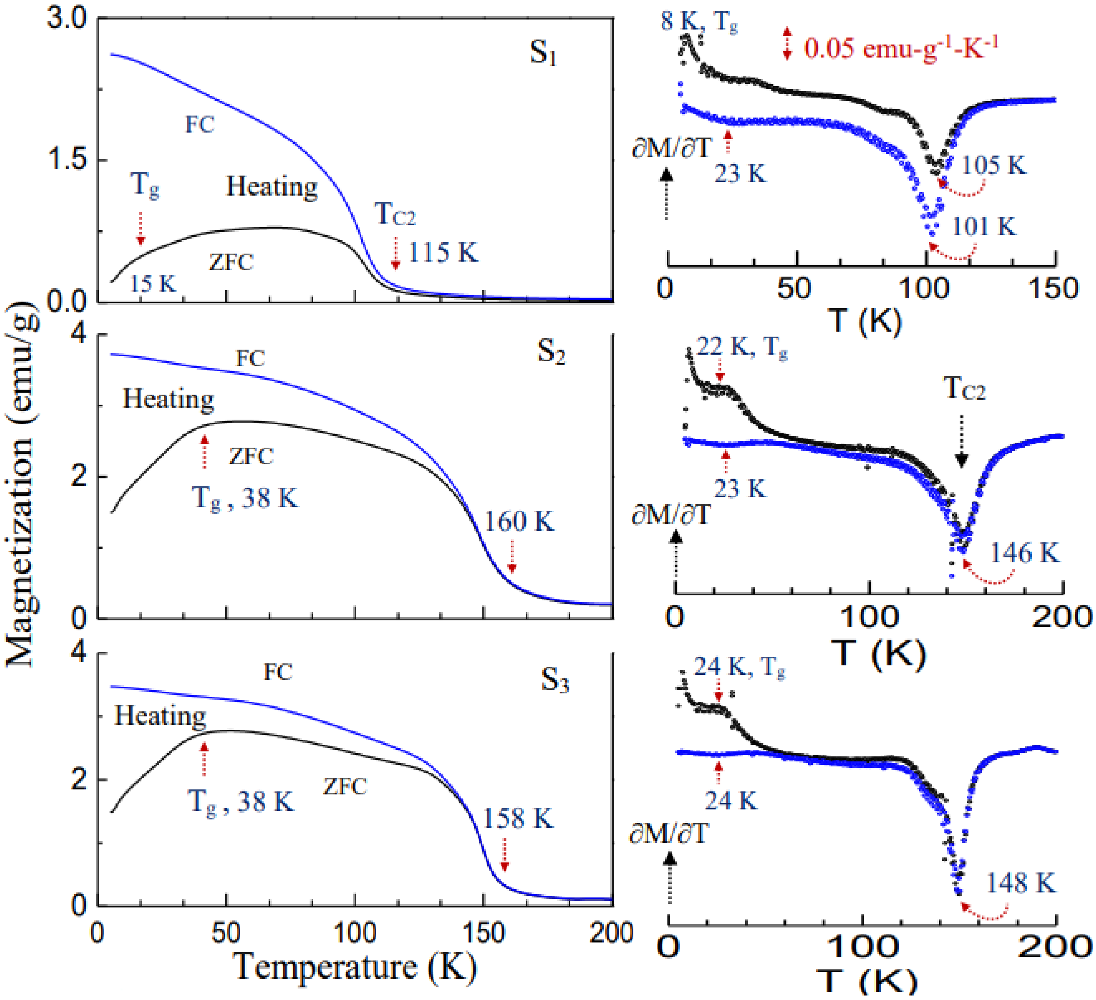

Fig. 3.8 ZFC–FC thermomagnetic curves of LNMO samples S_1, S_2, and S_3 over 5 - 200 K (at H = 100 Oe), exhibiting a sharp T_{c2} peak in the derivatives (right) of its value rising in an exchange-coupled core-shell structure.

where k_B and h are the Boltzmann and Planck constants, respectively. Further, in the Boltzmann hypothesis, a lattice (or a cluster) of N atoms, occupying ‘r’ energy levels ε_1, ε_2, ε_3,—ε_r in n_1, n_2, n_3, —n_r numbers, acquires

$$\Omega S_c(T) \cong k_B ln\Omega_c(T), \tag{3.4}$$

with a probability function of its stability at a given temperature,

$$\Delta S_c(T) \cong \frac{N!}{n_1!+n_2!+n_3!+---n_r!}, \tag{3.5}$$

i.e. number of microstates in an ensemble of N = Σn_i and energy E = $\Sigma \varepsilon_i n_i$. In fact, a sample has large numbers of small structures (building blocks) ordering one another at a larger scale of an optimized ΔS_c value [124, 125]. That dominates on multiple surfaces in small core–shells. At a temperature, only active phonons that exchange heat share a ΔS_v value. Thus, T_{SG} freezes as early 8 K in fine clusters, and mobilizes to 24 K in bigger entities. In eq. (3.3), a phonon $\nu \cong 530$ cm^{-1} of LNMO [94, 104] share ΔS_v = 2.6 J mol^{-1} K^{-1} at $T_{SG} \cong 24$ K, while 0.9 J mol^{-1} K^{-1} at $T_{SG} \cong 8$ K, which in turn using eq. (3.2) average ΔS_c = 3.4 J mol^{-1} K^{-1} and ΔH_{vc} = (-) 20.4 J mol^{-1} in a 8–24 K narrow band, or $\Omega \sim 1.5$ in eq. (3.4). Consistently, a similar $\Delta S_m \cong 35.1$ J mol^{-1} K^{-1} is reported at 20 K in a Gd_2CoMnO_6 cluster [121]. Derived from eq. (3.2), $(\partial H_{vc}/\partial T)_P \equiv C_P \cong \Delta S_v - \Delta S_c$,the part ΔS_c orders ($\Omega_c \rightarrow 1$) in ε_r a way to nullify ΔS_v on $C_P \rightarrow 0$ as $T \rightarrow 0$ (the third law of thermodynamics). Otherwise, it rises in soft phonons (also spins) cool, lose the kinetic energy, and converge onto the E_0 state (zero-point-energy).

Figures (3.9(a-c)) compare ZFC-FC curves of lower spin phase-1, which contain an order of lower M-H and shift oppositely to that of phase-2 (Fig. (3.8)) over lower 150–280 K temperatures on going S_1-S_3 samples. Primary T_{c1} signal at 234 K in sample S_1 (Fig. (3.9(a))) contains a satellite $T_{c1}{}^*$ signal (weak) at a higher value 260 K, a better N_1N_2 spin exchange-interaction. As $T_{c1}{}^*$ signal comes down it loses irreversibility in lesser surface spins on larger crystallites in S_2 and S_3 samples. A residual $T_{c1}{}^*$ is visible in the $M^* = \partial M/\partial T$ plots (at right to Fig. (3.9)) at 256 K and 251 K over coupled T_{c1} signal at 198 K and 191 K, respectively.

Table 3.3 Tailored spin-transitions and M_s, and H_c values of small core-shell LNMO crystallites.

Sample	Magnetic transitions*				M_s	H_c	Ref.
	T_{SG} (K)	T_{c2} (K)	T_{c1} (K)	$T_{c1}{}^*$ (K)	(emu/g)	(Oe)	
S_1	8 (23)	105 (101)	234	260	30.5	205	
S_2	22 (23)	146 (146)	198	256	53.8.	130	Present
S_3	24 (24)	148 (148)	191	251	52.7	125	
Bulk	42 (42)	-	270	-	56.8	300	[26, 103]
Nanoplates	52	102	284	-	17.6	≤ 500	[94]
Nanorods	20	-	178	-	72.2	130	[65]
Films	-	138	270	-	55	≥ 250	[95]

A lowered T_{c2} value, which arises in an electron $Ni^{2+} \rightarrow Mn^{4+}$ transfer, indicates a weaker Ni^{3+}-O^{2-}-Mn^{3+} superexchange interaction despite a larger ρ_s in this FM phase-2. It is exchange-coupled with FM phase-1—a 29 % lower ρ_s, but a bit larger T_{c1} value. So, it promotes T_{c2} on its combined M_2 value in S_1, S_2, and S_3 samples in counterpart M_1 field of phase-1 in the ZFC-FC curves in Figures (3.8) and (3.9). Thus, larger the M_2

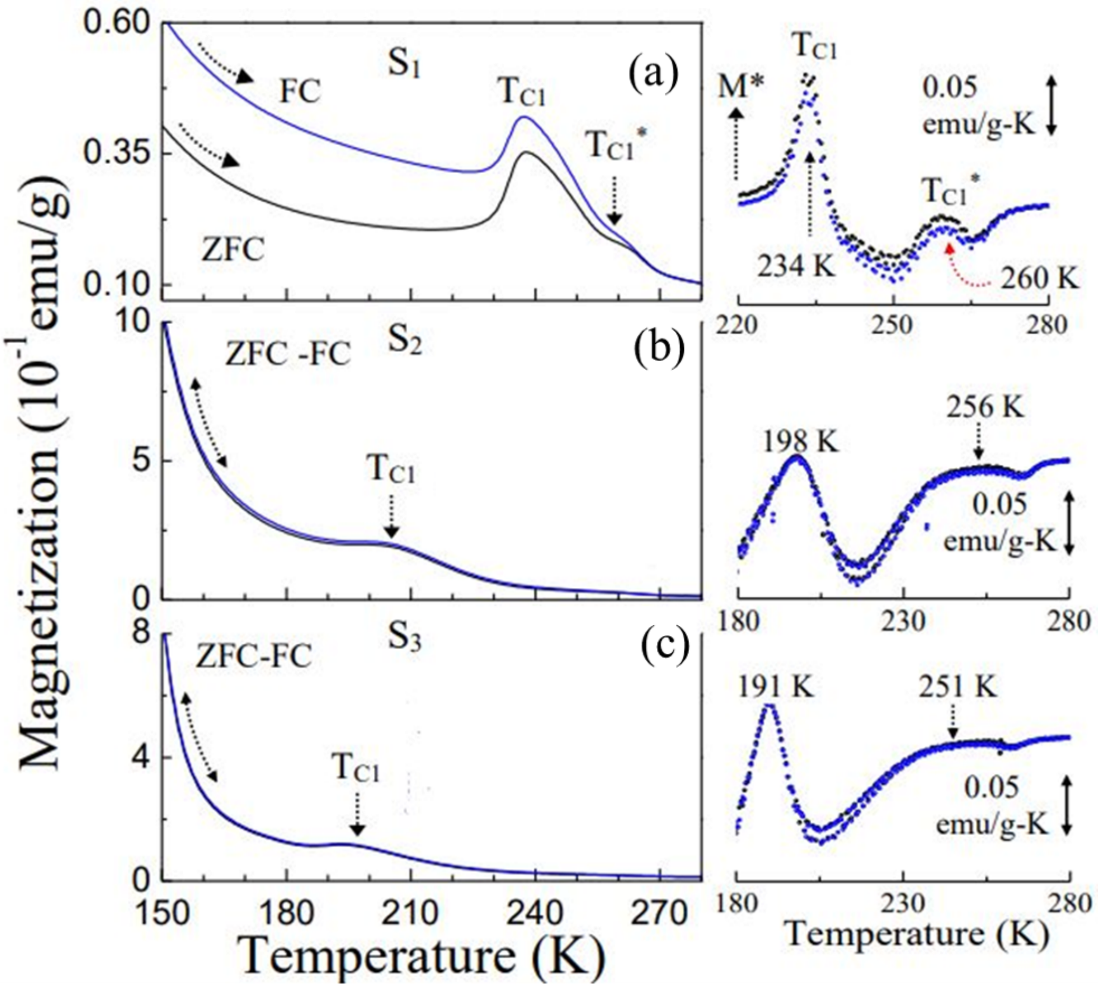

Fig. 3.9 Irreversibility in ZFC–FC curves of LNMO samples S_1, S_2, and S_3 over 150 - 280 K (at H = 100 Oe), showing how T_{c1} and T_{c1}* peak values in the derivatives (right) fall down on decreasing an antisite disorder.

larger T_{c2} in a model relation, $T_{c2} = \beta M_2 + C$, with a coupling coefficient $\beta \cong 31.9$ K g emu^{-1} and a correlation content C $\cong$ 81.1 K. A soft magnet ($\leqslant$ 10 vol %) defused in a hard magnet at the nanoscale is known to promote a net M-value of an exchange-coupled magnet [126, 127]. Uniquely, a LNMO ‘exchange-coupled over its inbuilt FM phases in a coupled spin-lattice controls its features. This kind of an electron doping promotes the T_{c2} value [128]. It opens a room to tailor valued properties on doping soft ferrites [129, 130] for uses at room temperature.

Figure (3.10) depicts the temperature-dependent magnetization loops. At low-temperature, samples have ferromagnetic kind nature, as shown in the Fig. (3.10). The temperature from (10 K $\rightarrow$ 100 K) or below T_{c2} samples have completely ferromagnetic nature, while at 100 K & 150 K (or in range of T_{c2} to T_{c1}) have paramagnetic kind nature. The room temperature

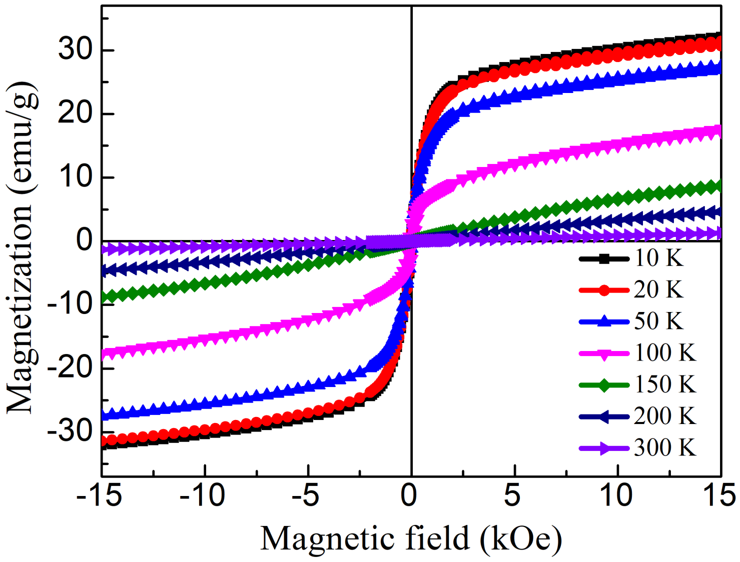

Fig. 3.10 Magnetic hysteresis loops of LNMO samples S_1 at different temperatures (10 K, 20 K, 50 K, 100 K, 150 K, 200 K, 300 K.)

samples have paramagnetic nature with a low moment. At 200 K and 150 K, magnetization value increases which suggests some magnetic ordering (ferromagnetic due to cations ordering), but dominating nature is paramagnetic (due to unordered spin) or antiferromagnetic (due to antisites). This compound has a competing ferromagnetic/antiferromagnetic nature which changes with external stimuli (temperature and magnetic field). It also confirms that Ni^{3+}-O^{2-}-Mn^{3+} dominating than Ni^{2+}-O^{2-}-Mn^{4+}.

3.2.4 Collective spin dynamics in core-shell crystallites

As given in Table (3.3), a spin-glass freezing, $T_{SG} \leqslant 42$ K, prevails in LNMO in field-dependent dc magnetization. Now, we explore the spin-cluster dynamics using frequency and temperature-dependent ac magnetic susceptibility, $\chi_{ac}(\omega, T)$, which also helps to identify blocking temperature reported in ZFC–FC dc magnetization [39, 131, 132]. In $\chi(\omega, T)$ studies, a time varying, sinusoidal magnetic field, $H_{ac} = 100$ Oe, has applied to probe the ground state of spins in small H_{ac} fields. A net field H acting on the sample can be given as $H = H_{dc} + H_{ac}\cos(\omega t)$, where $\omega = 2\pi f$ is angular frequency of oscillating H_{ac} field. Typically, the frequency lies in a 0.1–10^4 Hz range, so as to allow probing multiple dynamical processes. Thus, the results help analyzing multiple relaxations and energy barriers.

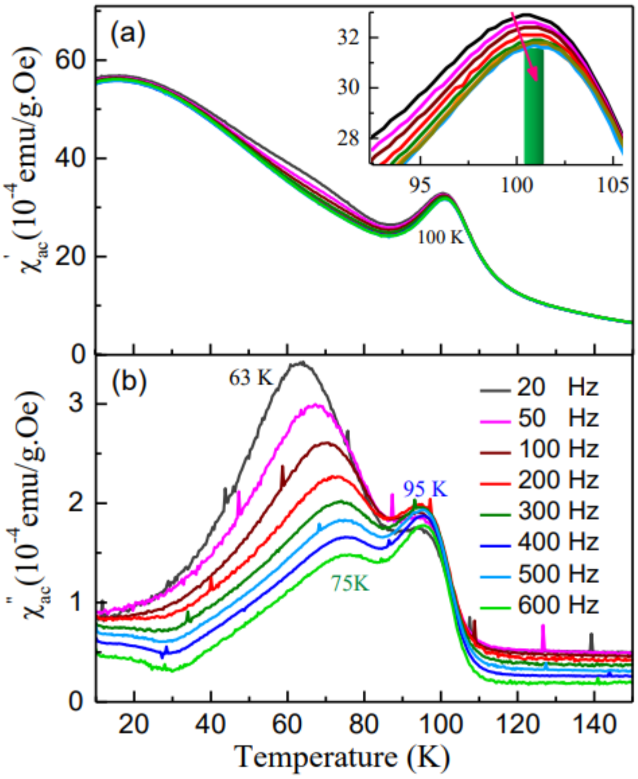

Fig. 3.11 Temperature dependence of (a) χ'_{ac} and (b) χ''_{ac} of sample S_1 measured at various frequencies 20 to 600 Hz (given in the inset) at an applied ac-drive field of 200 Oe. The inset panel shows an enlarged χ'_{ac} part across 100 K.

Figures (3.11(a & b)) display temperature variations of real (χ'_{ac}) and imaginary (χ''_{ac}) parts of χ_{ac} measured (sample S_1) over 10 –150 K at different frequencies, $\leq$ 600 Hz. A sharp χ'_{ac} peak observed at 100.4 K at 20 Hz has a small shift over higher temperatures, $\leq$ 1.0 K, on larger f $\leq$ 600 Hz, as highlighted in the inset (Figure (3.11(a))). A frequency-dependent T_{SG} signal is common in spin-glass and other likewise metastable phases. A Mydosh parameter, $\Omega = (1/T_{f(\omega)})*(\Delta T_{f(\omega)})/(\Delta \ln\omega)$ is used to distinguish the origin of spin relaxation and its dynamics. Here, ΔT_f (ω) is the peak shift with increased frequencies. In a case of magnetic frustration induced by cluster glass freezing, Ω spans across 0.005–0.09, while it usually ranges 0.1–0.3 for SPM species. Ω = 0.0017 estimated in this example suggests a frequency χ'_{ac} dispersion mainly arises from the cluster spin-glass freezing. Possibility of any SPM species and associated spin relaxation is ruled out. Further, two peaks have aroused at $\sim$ 65 and 95 K in the χ'_{ac} plots (Figure (3.11(b))), whereas the first peak (prominent) has more clearly shifted from 63 to 75 K and has regularly decreased intensity on larger frequencies. Thus, it looks weaker over the other peak at f $\geq$ 300 Hz.

Possibly, two signals arise from two types of spin clusters present in the core and shells, respectively.

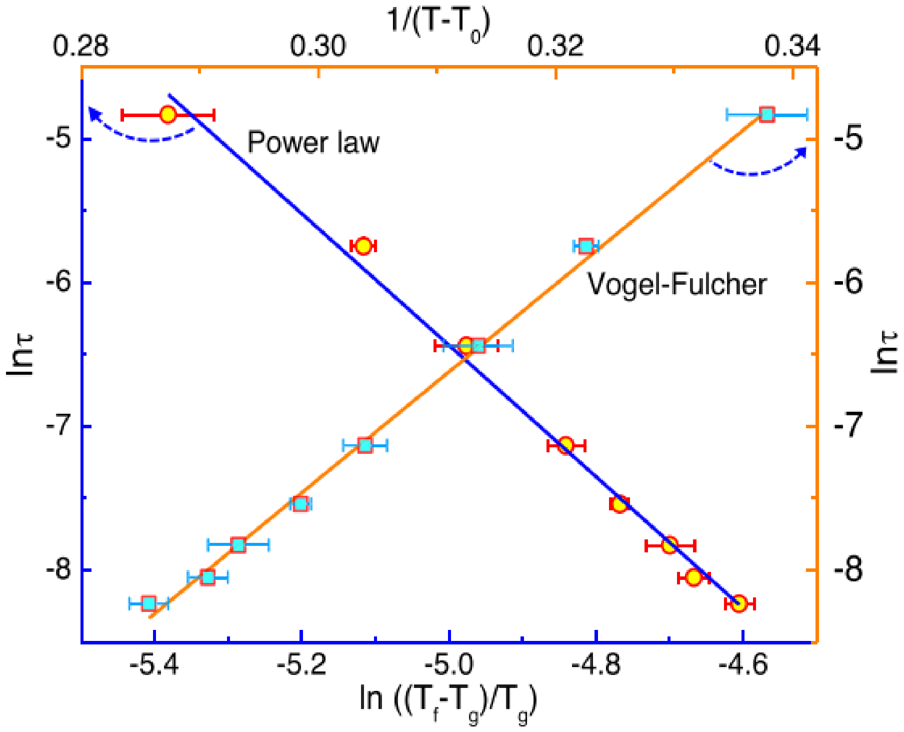

Fig. 3.12 (a) ln(τ) versus ln(T$_f$/T$_{SG}$ - 1) and 1/(T-T$_0$) plots for sample S$_1$, wherein the solid line represents the least squares fit for critical power law and Vogel-Fulcher law.

Two different theoretical models have been applied to explore a relationship of ω with a characteristic relaxation time (τ) for the LNMO crystallites. A temperature-dependent average value $\langle\tau(T)\rangle$ can be used to identify its intrinsic dynamics. Such scenario is presented to explain the Vogel–Fulcher law [39, 132] that describes the slowing down of relaxation behavior and freezing processes in many glass species,

$$\tau^{-1} = \tau_0^{-1} exp[(-E_a)/(k_B(T-T_0))] \tag{3.6}$$

where E$_a$ is an energy barrier, τ_0 is a microscopic attempt rate, and T$_0$ is an ordering temperature. The Vogel–Fulcher law assumes that relaxation processes are local and satisfies an Arrhenius law of activation energy E$_a$, which is determined by the energy required to overcome a local potential well. Thus, in this example, τ_0 = 9.3 × 10^{-13} s, E$_a$ = 5.8 meV mol^{-1} and T$_0$ = 97.5 K are obtained from the plot in Fig. (3.12).

We could model the temperature dependence of $\langle\tau(T)\rangle$ corresponding to T$_f$ peak temperature at each frequency. A value $\langle\tau(T)\rangle$ in power-law dynamics, commonly used in spin-glass systems, is determined using τ = 1/2πf. A power-law predicts a critical slowing down of the spin dynamics and its divergence at T_{SG} used to model the frequency dependence of the spin-glass freezing temperature T_f. The divergence can be modelled at T_{SG} through $\tau = \tau_0 \left(\frac{T_f - T_{SG}}{T_{SG}}\right)^{-z\nu}$, where τ_0 is the equilibrium τ value, T_{SG} is the spin-glass transition temperature at which τ diverges, and z is the dynamical critical exponent for correlation length ξ. A large τ_0 value governs slow dynamics as expected for cluster spin glasses, in which it typically lies at a scale 10^{-6} –10^{-10} s. For canonical spin-glasses, like AuFe, it is $\sim 10^{-13}$ s, suggesting a spin-glass nature. A least-square fit to the ln(τ) versus ln(T_f /T_{SG} - 1) plot shown with a solid line in Fig. (3.12) gives T_{SG} = 100 ± 0.4 K, τ_0 = 1.87×10^{-13} s, and $z\nu$ = 4.57 ± 0.04. Obviously, the frequency dispersion is mainly caused due to freezing of a cluster spin-glass in this example.

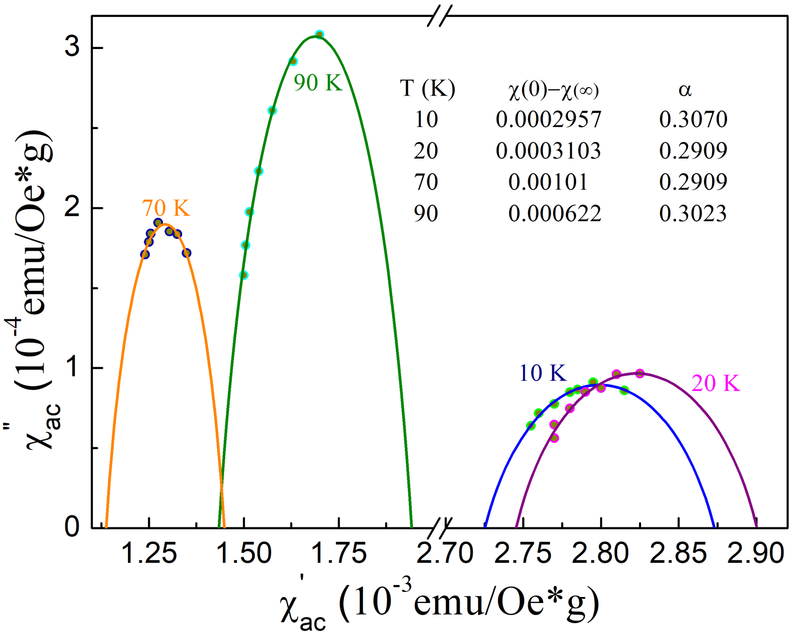

T (K)	χ(0)−χ(∞)	α
10	0.0002957	0.3070
20	0.0003103	0.2909
70	0.00101	0.2909
90	0.000622	0.3023

Fig. 3.13 Cole-Cole plot for the magnetic susceptibilities of the crystallites S_1.

We employed Cole-Cole formalism for quantitative analysis of spin dynamics [40, 133, 134]. This formalism helps in identifying the characteristics of relaxation time and its distribution.

$$\chi(\omega) = \chi(\infty) + \frac{\chi(0) - \chi(\infty)}{1 + (i\omega\tau_0)^{(1-\alpha)}} \tag{3.7}$$

where $\chi(0)$ and $\chi(\infty)$ are isothermal and adiabatic susceptibilities, ω is the angular frequency, and τ_0 is characteristics of relaxation time, α represents the parameter that implies the distribution of relaxation time [133–135]. The α values range between 0 and 1, corresponding to the mono and polydisperse relaxations. The formalism in Eq. (3.7) interrelates χ' and χ'' are deduced: $\chi''(\omega) = \text{-B}_0 + \left[B_0^2 + A_0\left(\chi'(\omega) - \chi''(\infty)\right) - \left(\chi'(\omega) - \chi''(\infty)\right)^2\right]^{1/2}$, where $\text{A}_0 = \chi(0) - \chi(\infty)$ and $\text{B}_0 = \text{A}_0.\tan(\pi\alpha/2)/2$. The relaxation dynamics of LNMO crystallites have also been studied through Argand diagrams [133–136]. In Cole-Cole plots for different temperature-independent parameters, A_0 and α correspond to the equation of a circular arc centered at the maximum where $\omega\tau_0 = 1$. The resulting Cole-Cole plots for multiple temperatures for sample S_1 as shown in Figure (3.13), where ac-susceptibility data are plotted for the selected frequency. The Cole-Cole plots for one relaxation process are symmetric and centered at $[\chi(0) + \chi(\infty)]/2$, where χ'' is maximum. As the parameter α is proportional to the ratio of the bottom width to the height of the curves, the plots are direct evidence of a distribution of relaxation times [40, 134, 137]. The plots fall on a circular arc as expected by the above equation and are well described for all magnetic fields, where the equation does not give a consistent result for both, as witnessed by the different values of A_0 and α. The different values of α support that different spin glass clusters show different relaxation mechanisms and times. As per magnetic properties studies, different magnetic interactions and spin states have different relaxation times or polydispercive behaviour (non-Debye) that agree with the analysis of the Cole-Cole plot.

3.2.5 Spin dynamics

Figure (3.14) shows the asymmetric broad line ESR spectra recorded at 298 and 80 K for crystallites S_1, S_2, and S_3. These spectra fitted using a linear combination of symmetric and an antisymmetric Lorentzian function given by,

$$S_{MOD} = K_1 \frac{(\frac{\Delta X}{2})(X - X_{RES})}{((X - X_{RES})^2 + (\frac{\Delta X}{2})^2)^2} + K_2 \frac{(\frac{\Delta X}{2})^2 - (X - X_{RES})^2}{((X - X_{RES})^2 + (\frac{\Delta X}{2})^2)^2} + offset + X.slope \tag{3.8}$$

where X_{RES}, ΔX define as the magnetic resonance field and peak-to-peak line width, K_1 and K_2 are asymmetric constants. Table (3.4) shows the fitted parameter related to the equation. At 298 K, LNMO crystallites are in a paramagnetic state, as evident from a narrow ESR spectrum. Fig. (3.14(a, b, & c)) represents the comparison of ESR spectra recorded at 298 K for S_1, S_2, and S_3. The estimated g-values for S_1, S_2, and S_3 are 2.050, 2.048, and 2.037, respectively. The decrease in the Lande g-value suggests a decrease in spin-orbital coupling. Figure (3.14(d, e, & f)) compares ESR spectra collected at 80 K for S_1, S_2, and S_3. At 80 K, reported line widths are broader compared to 298 K,

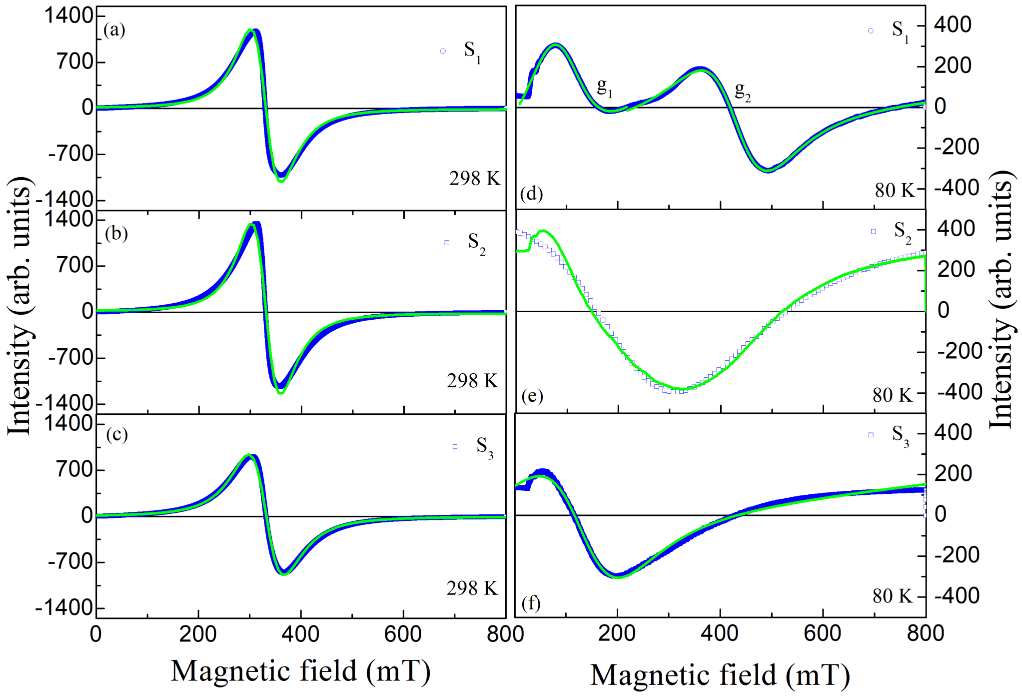

Fig. 3.14 (a, b, c) ESR spectra at 298 and (d, e, f) at 78 K for S_1, S_2, S_3 crystallites blue colour represent the raw data and green colour represent the fitted data.

indicating the presence of a collective relaxation phenomenon and spin glass nature at lower temperatures. The line width (ΔX), which is directly related to the spin relaxation process of the system, increases at lower temperatures [133, 135]. The spin freezing process at a lower temperature increases the ΔX. The Lande g-factor of any system depends on the crystal field splitting and spin-orbit coupling. Unlike lower temperatures, at 298 K, all the spins in LNMO crystallites can adopt a unidirectional orientation under the influence of an external magnetic field giving rise to a single g-value.

3.3 Conclusion

A core-shell LNMO (2–3 nm shell thickness) has grown in multiple facets of small crystallites (average size tuned from 65 to 80 nm) on reactive sintering of a powder (wet milled after a solid-state reaction) in ambient air. In a model reaction, the milling creates vital fractured surfaces, which conduct over (as a template) diffusion reactions so as to grow in coherent facets, namely, ⟨002⟩, ⟨200⟩, ⟨112⟩, of long lattice arrays. Surface spins, as setup at different angles on different facets in a canted structure, have a coupled spin dynamics—a ‘hierarchical spin cluster’. In turn, a high-spin cluster, $\rho_s = 0.7$ s a^{-1}, reforms

Table 3.4 ESR fitting parameter at 300 K and 80 K for LNMO crystallites. Symbol (*) represents the parameter related to g_1.

Parameter	Sample S_1			Sample S_2		Sample S_3	
	298 K	80 K*	80 K	298 K	80 K	298 K	80 K
Δ X	101.8	204.55*	432.91	98.39	617.66	118.72	279.57
X_{RES}	328.95	89.04*	230.34	329.36	232.92	331.16	131.98
g-value	2.05	7.36*	1.513	2.048	2.815	2.037	4.969
K_1	-9.28×10^6	$-3.53\times10^{6*}$	-1.06×10^7	-9.66×10^6	-9.38×10^7	-9.93×10^6	-1.62×10^7
K_2	2.87×10^5	$3.58\times10^{6*}$	-6.27×10^5	3.31×10^5	-4.69×10^7	2.33×10^5	-9.52×10^5

on an electron transfer Ni^{2+}-O^{2-}-$Mn^{4+} \rightarrow Ni^{3+}$-$O^{2-}$-$Mn^{3+}$ (phase-2) from a low spin ρ_s = 0.5 s a^{-1} phase-1. It anticipates the magnetic properties, a maximum M_s = 53.8 emu g^{-1} value (closer to a truly ordered phase-1, M_s = 56.8 emu g^{-1}) [61], with H_c = 130 Oe and K_1 = 2.5 × 10^6 erg cm^{-3}, i.e. a newer phase. Any local disorder lowers M_s, till 13.3 emu g^{-1} reported in bulk [103], or 17.6 emu g^{-1} in a nanostructure [94]. Its Curie point T_{c2} lies below that of T_{c1} in phase-1 of an 'exchange coupled' magnet of a 'double super-exchange interaction'. In a result, it caringly rises (105 – 148 K) closer to T_{c1} (234 – 191 K) as net surface spins (of a distinct $T_{c1}* > T_{c1}$, drops (260 – 251 K) lower in bigger crystallites. A combined effect governs the features in a type of electron doping like Ni^{2+} ions and/or O^{2-} vacancies.

The dynamics of spins in LNMO at low temperature is described using macroscopic and microscopic probes. A spin-glass phase, $T_{SG} \leq 25$ K, appears in dc magnetization of hysteric irreversibility. The χ_{ac} follows power-law/Vogel– Fulcher-type critical spin dynamics at a time scale of $\tau_0 \sim 10^{-13}$ s, suggesting a glassy spin-cluster phase coexists below $T_{SG} \sim 100$ K. Two $\chi_{ac}^{'}$ peaks appear at 65 K (broad) and 95 K (sharp) on regularly varied positions and intensity with frequency, 20–600 Hz, in two types of major spins. Below freezing temperature, ESR spectroscopy measurements suggest that core-shell structured LNMO crystallites manifest a collective relaxation process as evident from enhanced line-width and reduced g-value across the spin-glass phase. Cole-Cole plots as a function of temperature indicate that the magnetization relaxation is a dispersive process across spin-freezing. Our findings provide a pathway to tune the interfacial anisotropy of core-shell crystallites. The profound results have open scope of duly tuning spintronics over $\langle 112 \rangle$ anisotropic facets, multiple charge carriers, O^{2-} vacancies, and/or $Mn^{4+} \leftrightarrow$

Ni^{2+} antisites in small LNMO core–shells, useful to devise small magnets, tools, and other devices.